PAPER

Check for updates

Synthesis of a hollow MoSe$_2$@MXene anode material for sodium-ion batteries†

Hanbo Zou, [ID] *[a] Shaohao Li,[a] Wei Yang, [ID] [a] Quanbing Liu [ID] [b] and Shengzhou Chen [ID] *[b]

MXene and MoSe$_2$ as a novel two-dimensional transition metal carbide and selenide, respectively, are widely used in battery electrodes. In this study, MoSe$_2$ nanoflakes were grown *in situ* on hollow MXene spheres *via* a hydrothermal method. The obtained hollow 3D spherical MoSe$_2$@MXene composite exhibits outstanding rate performance and cycling stability as the sodium-ion battery anode. At a current density of 1 A g^{-1}, it achieves a specific capacity of 350.7 mA h g^{-1} after 1000 cycles with a retention rate of 93.7%. Even at a high current density of 10 A g^{-1}, the specific capacity remains at 224.2 mA h g^{-1}. The outstanding electrochemical performance of the MoSe$_2$@MXene composite is primarily attributed to the synergistic interaction between MoSe$_2$ and the MXene, which significantly reduces the self-aggregation of the MXene and MoSe$_2$ and effectively enhances the diffusion and migration rates of sodium ions.

Introduction

With the widespread use of portable electronic devices such as laptops and electric vehicles, lithium-ion batteries as the indispensable technology have experienced rapid development. However, owing to the limited lithium reserves, developing efficient alternatives to lithium-ion batteries has become crucial for the future energy system.[1–3]

Sodium has the advantages of abundant reserves, cost-effectiveness and physicochemical properties similar to lithium; thus it has great potential applications in energy storage and conversion.[4] However, the commercialization of sodium-ion batteries still faces certain issues.[5] First, the larger radius of sodium ions (1.02 Å) than that of lithium ions (0.76 Å) significantly reduces the structural stability and energy density of electrode materials.[6] Second, graphite, widely used as an anode material in lithium-ion batteries, has been found to be incompatible with sodium-ion batteries because of the larger sodium ions and smaller spacing between graphite layers.[7–9] Therefore, research and development of anode materials for sodium-ion batteries is of great importance.

In recent years, transition metal chalcogenides (MX$_2$: M = transition metal and X = S, Se, and Te) have received extensive attention in the field of energy storage owing to their unique physical structures and chemical properties.[10–15] Transition metal sulfides (*e.g.* MoS$_2$) have made significant progress as anode materials for batteries. Selenium and sulfur belong to the same main group; thus, the properties of transition metal selenides and sulfides are similar.[14,16] Owing to the higher density and conductivity of selenium, the volumetric energy density and rate capability of selenide electrodes may exceed those of sulfides. MoSe$_2$ is a two-dimensional layered material similar to graphene. The spacing of the Se–Mo–Se interlayer is about 0.65 nm, which is larger than that of sodium ions. Thus, the MoSe$_2$ electrode can facilitate the rapid insertion and extraction of sodium ions and deliver superior electrochemical performance with a theoretical specific capacity of up to 422 mA h g^{-1}.[11,17,18] However, because of the inherent low conductivity and agglomeration tendency of MoSe$_2$, pure MoSe$_2$ presents poor rate performance and cycling stability. To enhance the conductivity of MoSe$_2$, researchers have attempted various strategies such as combing selenides with carbon materials or constructing heterojunctions.[19,20] Zhang[21] synthesized MoSe$_2$/rGO composites *via* a hydrothermal method with a reversible capacity of 430 mA h g^{-1} at a current density of 0.5 A g^{-1}. The synergistic effect between MoSe$_2$ and graphene significantly improves the sodium storage performance. Chao[22] synthesized G-Cu$_2$Se@MoSe$_2$ nanosheets with dual heterojunctions by a hydrothermal method. G-Cu$_2$Se@MoSe$_2$ with this special structure provides a capacity of 288 mA h g^{-1} at 50 A g^{-1} and 89.6% capacity (291 mA h g^{-1}) after 15 000 cycles at 10 A g^{-1}.

MXenes are the novel two-dimensional transition metal carbides, which possess excellent properties such as high metallic conductivity,[23,24] large specific surface area,[25] and abundant

[a]Guangzhou Key Laboratory for New Energy and Green Catalysis, Guangzhou University, Guangzhou 510006, China. E-mail: szchen@gzhu.edu.cn
[b]School of Chemical Engineering and Light Industry, Guangdong University of Technology, Guangzhou, 510006, China. E-mail: liuqb@gdut.edu.cn
†Electronic supplementary information (ESI) available. See DOI: https://doi.org/10.1039/d5nr00156k

functional groups.[26] The outstanding conductivity facilitates rapid charge transfer, and the unique layered structure promotes the ion diffusion. Additionally, the large specific surface area enhances the interactions with other materials and reveals the significant potential in energy storage applications.[25] An MXene/MoSe$_2$ composite was synthesized by an *in situ* one-step hydrothermal method.[27] With the unique heterostructure and large specific area, MXene/MoSe$_2$ achieved a specific capacitance of 1358.5 F g^{-1} at 1 A g^{-1}, significantly higher than those of pure MXene and MoSe$_2$ electrodes. However, similar to other two-dimensional materials, MXene nanosheets tend to stack, restricting the diffusion and transfer of sodium ions. Two-dimensional MXene sheets were synthesized into three-dimensional hollow spheres by a template method.[28] The obtained hollow MXene microspheres delivered a reversible capacity of 295 mA h g^{-1} after 1000 cycles at a charging rate of 2.5 C. Even at a high charging rate of 25 C, the composite retained a discharge capacity of 120 mA h g^{-1}.

The construction of MXenes with hollow spherical structures can effectively improve the structural stability and the electrochemical performance.[11,19,29] This structure allows the electrolyte to fully penetrate into the hollow cavities and shortens the ion transport path.[29] In this study, two-dimensional MXene nanosheets were assembled into hollow MXene spheres using a template method, and then, MoSe$_2$ was anchored onto the hollow MXene spheres *via* a hydrothermal method, preventing the growth of nanosheets and agglomeration. The obtained MoSe$_2$@MXene composite demonstrated eminent cycling stability and rate performance for sodium-ion batteries.

Experimental

Chemicals

Titanium aluminum carbide (Ti$_2$AlC$_2$, 200 mesh, 98%), sodium molybdate dihydrate (Na$_2$MoO$_4\cdot$2H$_2$O, 98%), methacryloxyethyl trimethyl ammonium chloride (DMC, C$_9$H$_{18}$ClNO$_2$, 75 wt%), 2-methylpropionitrile (AIBN, CH$_{12}$N$_4$, 99%) and glucose (C$_6$H$_{12}$O$_6$, 99%) were purchased from Macklin. Lithium fluoride (LiF, 99%), concentrated hydrochloric acid (HCl, 37%), styrene (C$_8$H$_8$, 99.5%), hydrazinium hydrate solution (N$_2$H$_4\cdot$xH$_2$O, 80%) and selenium powder (Se, 99%) were purchased from Aladdin. No further purification was required for these reagents.

Preparation of single-layered MXenes (MXene-SL)

First, 2 g LiF was weighed and dissolved into 120 mL of 9 M HCl solution with stirring at room temperature for 15 minutes. Then, 2 g MAX powder was slowly added into the above solution in small portions to avoid overheating. The mixture was stirred at 55 °C for 48 hours, centrifuged and then washed several times with deionized water at 3500 rpm until the pH value of the supernatant reached approximately 6. The precipitate was redispersed into deionized water, sonicated for 30 minutes, and subsequently centrifuged at 3500 rpm for

1 hour. The resulting suspension was collected with a concentration of approximately 2 mg mL^{-1} and denoted as MXene-SL.

Preparation of MXene@polystyrene spheres (MXene@PS)

First, 13.6 g styrene was added into a flat-bottom flask containing 120 mL methanol and 30 mL deionized water, and then AIBN and DMC were sequentially mixed with a mass ratio of styrene, AIBN and DMC of about 50/1/1. The mixture was purged with nitrogen gas for 10 minutes to remove dissolved oxygen and then sealed for the reaction in an oil bath at 70 °C for 8 hours. The product was centrifuged and washed to obtain polystyrene (PS) spheres with an approximate diameter of 500 nm. Then 1 g PS spheres were dispersed into 80 mL deionized water, mixed with a 100 mL MXene-SL suspension solution (mass ratio of PS to MXene-SL is 5/1) and then stirred for 30 minutes. Finally, the suspension was centrifuged to remove unbound MXenes, and the product was freeze-dried to obtain greenish-black MXene@PS spheres.

Preparation of the hollow MoSe$_2$@MXene sphere

The preparation process of hollow-structured MoSe$_2$@MXene composites is illustrated in Fig. 1. First, 0.4 g MXene@PS spheres, 0.2 g glucose, and different amounts of Na$_2$MoO$_4\cdot$2H$_2$O were ultrasonically dispersed in 30 mL deionized water. Subsequently, Se powder with a Mo-to-Se molar ratio of 1/2.5 was mixed into 15 mL N$_2$H$_4\cdot$H$_2$O solution under constant stirring and heating to obtain a red-brown suspension. The resulting mixture was transferred to a 60 mL polytetrafluoroethylene (PTFE) – lined reactor, sealed in a stainless steel autoclave, and reacted at 200 °C for 24 hours. The black product was washed several times with deionized water and ethanol, vacuum-dried at 60 °C for 12 hours, and finally calcined in a tubular furnace at 550 °C for 1 hour at a heating rate of 5 °C min^{-1}. To investigate the effect of the MXene content on the performance of the composites, the MoSe$_2$@MXene samples with different mass ratios of MXene to MoSe$_2$ (10%, 20%, 30%, and 40%) were prepared and labeled as MoSe$_2$@MXene-10, -20, -30, and -40, respectively.
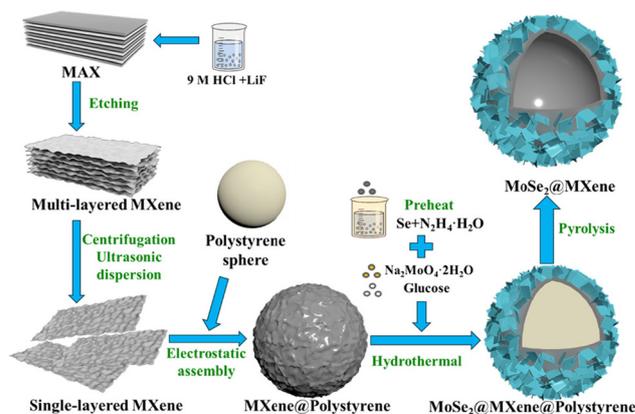

Fig. 1 Schematic of the synthesis of the hollow MoSe$_2$@MXene spheres.

Characterization methods

The crystal structures of the samples were identified through powder X-ray diffraction (PANalytical P3040/60) using Cu Kα radiation (λ = 1.5415 Å). Raman analysis was performed using an inVia Raman spectrometer with 523 nm laser light over the scanning range of 50–2000 cm^{-1}. Nitrogen adsorption–desorption measurements were performed using an ASAP 2020 instrument after degassing the samples at 150 °C for 4 hours. The morphology of the MoSe$_2$@MXene composites was examined by field emission-scanning electron microscopy (SEM, HITACHI-SU8010) and transmission electron microscopy (TEM, FEI Tecnai F20). The elemental distribution of the composites was further analyzed by energy-dispersive X-ray spectroscopy (EDS, Thermo Scientific K-Alpha). X-ray photoelectron spectroscopy (XPS) data were collected using a Thermo ESCALAB 250Xi spectrometer. The material compositions were determined using an inductively coupled plasma-optical emission spectrometer (ICP-OES, Optima 8300 ICP). The zeta potentials of the samples in the aqueous medium were measured – using a Zetasizer Nano analyzer (ZS920).

Electrochemical measurements

Polyvinylidene fluoride (PVDF), super P, and the active material were weighed in a mass ratio of 1/2/7 and then mixed uniformly with N-methyl pyrrolidone (NMP) as the dispersant. The resulting slurry was pressed onto the copper foil and dried at 60 °C for 12 hours. Circular electrodes with a diameter of 12 mm were punched from the coated foil and used as the anodes. The mass loading of the active material was maintained within 1.2–2 mg. The coin cells were assembled with the above electrode as the working electrode, a sodium metal sheet as the reference electrode, and 1 M NaPF$_6$ dissolved in EC/DEC (1 : 1 by volume) as the electrolyte. The assembly of the half-cells was conducted in an argon-filled glove box. Charge–discharge cycling and GITT measurements were performed using a NEWARE battery test system over the voltage range of 0.01–3.0 V. Electrochemical impedance spectroscopy (EIS) was performed using a Solartron electrochemical workstation (SI1287 + 1260) with an amplitude of 5 mV and a frequency in the range from 100 kHz to 0.01 Hz.

Computational method

Density functional theory (DFT) calculations were performed using the Vienna ab initio simulation package (VASP). The projector-augmented-wave (PAW) method and Perdew–Burke–Ernzerhof (PBE) function were employed to describe the electron–ion interactions and the exchange–correlation energy.[30,31] A plane-wave cutoff energy of 500 eV was applied, with an energy convergence criterion of 1×10^{-5} eV and a maximum final force threshold of 0.01 eV Å^{-1}. A 16 × 16 × 1 k-point mesh was used for the Brillouin zone. Additionally, a vacuum region of 15 Å along the z-direction was introduced to eliminate the periodic interactions.

Results and discussion

Multi-layered MXene (MXene-ML) with the typical accordion-like structure was successfully etched from MAX (Fig. S1a†) precursor with the mixture of HCl and LiF, as shown in Fig. S1b.† The single-layered MXene (MXene-SL) was exfoliated with ultrasonic treatment and centrifugation, as shown in Fig. 2a. MXene-SL exhibited a wrinkled morphology and superior stretchability.[32,33] As shown in Fig. 2b, the diameter of the as-fabricated polystyrene spheres (PS) is approximately 500 nm and the spherical surface is smooth. The zeta potentials of PS, MXene-SL, and MXene@PS are provided in Fig. S2.† It is evident that the PS spheres carry the positive charge, while MXene-SL is negatively charged due to the abundant active functional groups on its surface.[34] MXene@PS spheres exhibited a negative charge, and the zeta potential was lower than that of MXene-SL. For the MXene@PS sphere, MXenes were uniformly covered on the PS spheres via electrostatic assembly, as shown in Fig. 2d and e. Fig. 2f and g verify that the hollow MXene spheres were obtained after calcining MXene-PS spheres and removing the PS template. Although some MXene spheres were fragmented, the majority of MXene spheres still maintained the spherical-shell shape. This is due to the inherent bending resistance of the single-layered MXene and PS spheres preventing MXenes from stacking. Fig. 2h and i show that the MoSe$_2$@MXene-30 composite retains a more intact spherical structure than that of the hollow MXene spheres. MoSe$_2$ nanoflakes are observed to grow vertically on MXenes with the unique three-dimensional structure. This is attributed to the rich functional groups on the surface of MXene spheres, thus MoO$_4^{2-}$ ions can be adsorbed onto the surface of MXenes and then MoSe$_2$ was in situ synthesized during the hydrothermal process.[35] Without the MXene@PS template, the MoSe$_2$ samples exhibited spherical nanoflowers

Fig. 2 SEM images of (a) the MXene-SL, (b and c) PS sphere, (d and e) MXene@PS sphere, (f and g) hollow MXene sphere, and (h and i) MoSe$_2$@MXene-30. (j–j$_3$) TEM images of the MoSe$_2$@MXene-30 composite. (k–k$_4$) HRTEM images of the MoSe$_2$@MXene-30 composite and elemental distribution profiles of Mo, Se, Ti, and C.

with obvious self-aggregation (Fig. S1c and d†).[36] The addition of MXene@PS spheres effectively suppressed $MoSe_2$ aggregation and prevented the formation of stacked nanoflower structures. For the $MoSe_2$@MXene series composites (Fig. S1e–j†), the $MoSe_2$ layers became thinner and the arrayed structure of $MoSe_2$ was more pronounced with the gradual increase in MXene content. Notably, the hollow $MoSe_2$@MXene composites can serve as a container for the electrolyte and offer the buffering space to alleviate the volumetric expansion of $MoSe_2$ during the charge–discharge processes.[34]

The microstructure of the $MoSe_2$@MXene-30 composite was analyzed by transmission electron microscopy (TEM) test. In Fig. 2j–j_3, $MoSe_2$@MXene-30 displays a clear hollow spherical structure with a particle size of approximately 500 nm. The dark region within the spherical wall corresponds to MXene-SL, which further proves the complete removal of the PS template and the formation of a hollow structure. Additionally, the lattice fringe of 0.95 nm is attributed to the d-spacing of the (002) lattice plane for the MXene sample (Fig. 2j_2). It is demonstrated that the interlayer distance of MXene-SL increases during the exfoliation of MXene-ML.[37] Fig. 2j_3 shows that the $MoSe_2$ sheets are grown on the shell of the hollow MXene sphere. The lattice spacing is 0.65 nm corresponding to the (002) crystal plane of hexagonal 2H-$MoSe_2$.[11,22] To reveal the elemental distribution of the $MoSe_2$@MXene composites, energy-dispersive spectroscopy (EDS) analysis was performed, and the patterns are presented in Fig. 2k–k_4. It is shown that Ti and C elements are mainly distributed in the hollow sphere, while Mo and Se are mainly centered in the outer shell. It is illustrated that $MoSe_2$ is grown uniformly on the surface of hollow MXene sphere. In addition, the contents of Mo and Ti elements in four $MoSe_2$@MXene composites were measured by ICP-OES. As displayed in Table S1,† the $MoSe_2$ contents in these composites closely match the theoretical values with minor deviation.

The crystal structures of MAX, MXene-ML, MXene-SL, and $MoSe_2$@MXene composites were characterized by XRD, and are shown in Fig. 3a. The characteristic diffraction peak (104) of MAX was absent for both MXene and MXene-SL, indicating the complete etching of the Al layer from MAX and the successful synthesis of MXene. Furthermore, the (002) peak located at 9.5° for MAX shifted to 8.7° and 7.4° for MXene-ML and MXene-SL, respectively. Additionally, the diffraction peaks corresponding to the (004) and (006) planes of MXene-SL were observed, which revealed that MXene was successfully prepared[29] and the interlayer spacing of MXene increased progressively after the removal and exfoliation of the Al layer.[19,38] This enlarged interlayer spacing facilitated the rapid insertion and extraction of sodium ions. Fig. 3b presents the XRD patterns of pure $MoSe_2$ and $MoSe_2$@MXene composites with different $MoSe_2$ and MXene ratios. All samples exhibited characteristic peaks centered at 13.7°, 31.56°, 37.88°, and 56.35° attributed to the (002), (100), (103), and (110) planes of hexagonal 2H-$MoSe_2$ (PDF#29-0914), respectively.[20,22] It was demonstrated that PS template was removed completely after calcination and no impurity phases were introduced. Notably,
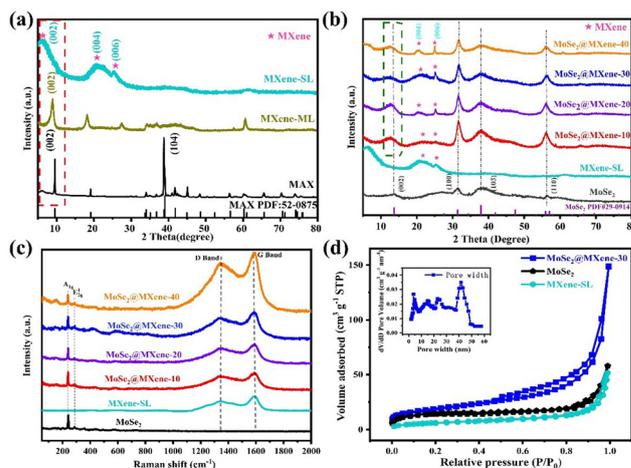
Fig. 3 (a) XRD patterns of MAX, MXene-ML and MXene-SL. (b) XRD patterns of $MoSe_2$, MXene-SL and $MoSe_2$@MXene series composites. (c) Raman spectra of the $MoSe_2$@MXene composites. (d) N_2 adsorption/desorption isotherms of $MoSe_2$, MXene-SL and $MoSe_2$@MXene-30 and pore size distribution curve of $MoSe_2$@MXene-30.

the (002) peak of $MoSe_2$ for the $MoSe_2$@MXene samples showed a significant leftward shift compared with that of pure $MoSe_2$, which indicated that the $MoSe_2$@MXene samples had larger $MoSe_2$ layer spacings than those of $MoSe_2$. The expanded $MoSe_2$ layers continued to gather into spherical nanoflowers, which is consistent with the above analysis with SEM images. As the MXene-SL ratios of $MoSe_2$@MXene composites increased, the intensity of the (004) and (006) peaks progressively enhanced.

The Raman spectra of pure $MoSe_2$, MXene-SL, and $MoSe_2$@MXene composites are shown in Fig. 3c. Pure $MoSe_2$ exhibits two distinct peaks at 241.5 cm^{-1} and 286.8 cm^{-1}, representing the out-of-plane A_{1g} and in-plane E^1_{2g} vibrational characteristics of Se.[11] The Raman peaks of MXene are located at 1344.0 cm^{-1} and 1591.0 cm^{-1} corresponding to the D and G bands of carbon vibrations, respectively.[39] The four peaks of the $MoSe_2$@MXene composites attributed to A_{1g} and E^1_{2g} vibrated peaks of Se element and the D and G vibrated bands of carbon, respectively. The successful *in situ* growth of $MoSe_2$ on MXene was further confirmed, which is in agreement with the XRD results.

The specific surface area is a crucial factor to the energy storage property of the electrode materials. N_2 adsorption–desorption analyses are performed for pure $MoSe_2$, MXene-SL and $MoSe_2$@MXene samples, and the results are displayed in Fig. 3d and Fig. S3.† It is revealed that all $MoSe_2$@MXene samples exhibit type III hysteresis loops in the curve. The specific surface areas of $MoSe_2$@MXene-10, -20, -30, and -40 composites are 28.84, 52.37, 71.13, and 37.49 m^2 g^{-1}, respectively, which are higher than that of pure $MoSe_2$ and MXene-SL. Notably, the $MoSe_2$@MXene-30 composite achieved the highest specific surface area, approximately 3.26 times that of pure $MoSe_2$ (21.8 m^2 g^{-1}) and 4.9 times that of MXene-SL (14.51 m^2 g^{-1}), which is due to the vertical growth of $MoSe_2$

nanoflakes on MXene template spheres and the formation of the unique three-dimensional array structure. The large specific surface area and broad mesoporous distribution (4–50 nm) of MoSe$_2$@MXene-30 facilitate the rapid transport of Na$^+$ ions.

The chemical composition and interfacial characteristics of MoSe$_2$@MXene-30 composite were characterized by X-ray photoelectron spectroscopy (XPS) analysis. The survey spectrum in Fig. 4a reveals the presence of Mo, Se, Ti, C, and O elements, which is in accordance with the EDS results. As shown in Fig. 4b, the high-resolution Mo 3d spectrum displays three main peaks at 228.4 eV, 231.6 eV, and 234.7 eV, respectively. The first two peaks are attributed to the 3d$_{5/2}$ and 3d$_{3/2}$ peaks of Mo^{4+} species, respectively.[27] While the last peak at 234.7 eV corresponds to Mo–O bond, which is indicative of the electron exchange between the MXene and MoSe$_2$.[40] The Se 3d XPS spectrum shows two distinct peaks at 53.9 eV and 54.9 eV assigned to Se 2d$_{5/2}$ and Se 2d$_{3/2}$, respectively.[27,37] Ti 2p XPS spectra, as shown in Fig. 5d, display four distinct peaks located at 457.7, 463.8, 458.4, and 464.7 eV, corresponding to Ti^{3+} 2p$_{3/2}$, Ti^{3+} 2p$_{1/2}$, Ti–O 2p$_{3/2}$ and Ti–O 2p$_{1/2}$ orbitals, respectively.[11] Notably, it is reported that the characteristic peaks of Ti^{3+} species will vanish from the Ti 2p spectrum if the oxidation of MXene occurred.[41] Thus the presence of Ti^{3+} 2p$_{3/2}$ and 2p$_{1/2}$ peaks authenticates that the MXene nanosheets can still remain unoxidized during the synthesis process. The peaks of Ti–O species arise from the formation of Ti–O bonds between the MXene and oxygen-containing functional groups on the surface.[42] The C 1s XPS spectrum in Fig. 4e exhibits the characteristic peaks at 280.7, 283.3, and 284.8 eV, assigned to the C–Mo, C–Ti, and C–O bonds, respectively. The presence of C–Mo peak indicates the strong interaction between MoSe$_2$ and the MXene.[43]

The electrochemical behavior of the MoSe$_2$@MXene-30 composite was systematically investigated in sodium-ion batteries. Cyclic voltammetry (CV) measurements were performed in the voltage window of 0.0001–3 V (vs. Na/Na$^+$) at a scan rate of 0.1 mV s^{-1}. As shown in Fig. 5a, the CV curves of the MoSe$_2$@MXene-30 composite for the first two cycles exhibit
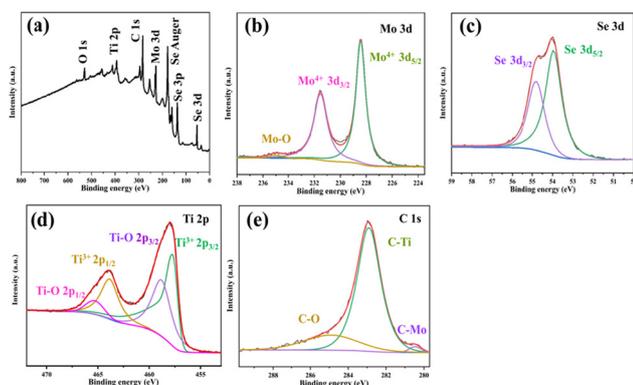
Fig. 5 (a) CV curves of MoSe$_2$@MXene-30 at a scan rate of 0.1 mV s^{-1}. (b) Cycling performance of MoSe$_2$ and different MoSe$_2$@MXene samples at 1 A g^{-1}. (c) Rate performance of MoSe$_2$ and MoSe$_2$@MXene composites at different current densities. (d) Long-term cycling discharge capacities and coulombic efficiencies of MoSe$_2$@MXene-30 at different current densities of 0.5, 1.0, and 2.0 A g^{-1}.

significant differences. The discrepancy is primarily attributed to the formation of SEI films during the first cycle.[43,44] In the initial cycle, two cathodic peaks are observed at 0.75 V and 0.45 V, respectively. The former peak is ascribed to the initial intercalation of sodium ions into MoSe$_2$ layers, while the latter peak at 0.45 V is associated with the conversion of Na$_x$MoSe$_2$ into metallic Mo and Na$_2$Se, along with the formation of the SEI layer.[37,43] Two anodic peaks are observed at 0.4 V and 1.7 V owing to the deinsertion of sodium from Na$_2$Se and Na$_x$MoSe$_2$, respectively.[27,45] In the second and third cycles, the redox peaks appear nearly at the same positions as the first cycle, indicating the excellent cycling stability of the MoSe$_2$@MXene-30 composite. Notably, in the second cycle, two additional cathodic peaks emerged at 1.37 V and 0.7 V, corresponding to the intercalation of sodium ions into Se after the formation of SEI layer, namely the reduction of Se to Na$_2$Se$_x$ and Na$_2$Se$_x$ to Na$_2$Se, respectively.[43,46,47]

The rate performance of pure MoSe$_2$ and MoSe$_2$@MXene series composites was evaluated in the current density range of 0.1–10 A g^{-1} (Fig. 5c). The results demonstrate that MoSe$_2$@MXene composites exhibit superior rate performance to pure MoSe$_2$, whether at low or high current densities.

Fig. 4 XPS profiles of MoSe$_2$@MXene-30 composites: (a) full spectrum, (b) Mo 3d, (c) Se 3d, (d) Ti 2p, and (e) C 1s.

MoSe$_2$@MXene-30 composite displays the best electrochemical performance. At current densities of 0.1, 0.2, 0.5, 1.0, 2.0, and 3.0 A g^{-1}, it delivers specific capacities of 415, 385, 376, 355, 346, and 332 mA h g^{-1}, respectively. Even at high current densities of 5.0, 7.0, and 10.0 A g^{-1}, the specific capacity can remain 301, 268, and 230 mA h g^{-1}, respectively. Remarkably, when the current density drops back to 0.1 A g^{-1}, the reversible capacity can restore 421 mA h g^{-1} without any capacity fading. These results further prove that MoSe$_2$ supported on hollow MXene spheres not only significantly improves the poor electrical conductivity of MoSe$_2$, but also enhances the structural stability. Thus, MoSe$_2$@MXene composites show excellent cycling properties and rate performance at high current density.

Fig. 5b manifests the cycling performance of pure MoSe$_2$ and four different MoSe$_2$@MXene composites at a current density of 1 A g^{-1}. The initial reversible capacity of the pure MoSe$_2$ electrode is 319.6 mA h g^{-1}. However, after 1000 cycles, the capacity of the MoSe$_2$ electrode sharply declines to 41.8 mA h g^{-1}, with only 13.1% retention rate of the initial capacity. The remarkable degradation is attributed to the agglomeration of the flower-like MoSe$_2$ nanostructures. The edges of MoSe$_2$ nanoflakes gradually fracture during the cycling, which causes a rapid decrease in electrochemical performance. In contrast, MoSe$_2$@MXene-10, -20, -30, and -40 electrodes exhibit retention rates of 42.1%, 89.6%, 93.7%, and 80.9%, respectively, after 1000 cycles. Notably, the MoSe$_2$@MXene-30 electrode demonstrates the best cycling stability, with an initial capacity of 374.3 mA h g^{-1} and a high reversible capacity of 350.7 mA h g^{-1} after 1000 cycles.

To further evaluate the cycling stability of MoSe$_2$@MXene-30 composite, cycling tests are conducted at different current densities (Fig. 5d). At a current density of 0.5 A g^{-1}, the electrode reaches an initial reversible capacity of 386.5 mA h g^{-1} and maintains the capacity of 367.6 mA h g^{-1} after 1000 cycles, corresponding to the retention rate of 95.1%. At a higher current density of 2 A g^{-1}, the capacity decreased slightly from the initial 292.3 mA h g^{-1} to 261.1 mA h g^{-1} after 1000 cycles, with a retention rate of about 89.1%. Hollow MXene spheres not only serve as a robust bracket to mitigate the agglomeration of MoSe$_2$ nanoflakes but also reduce the size of the MoSe$_2$@MXene-30 sample, which can enhance the interaction between the MoSe$_2$@MXene-30 electrode and the electrolyte and promote exceptional cycling stability.[37,48] However, MoSe$_2$@MXene-10 fails to effectively alleviate the agglomeration issues of MoSe$_2$ due to the low MXene content, resulting in relatively poor cycling stability. Similarly, MoSe$_2$@MXene-40 composites with low proportion of MoSe$_2$ possess significantly low capacities due to insufficient active material. The incorporation of MXene substantially enhances the electrochemical performance of MoSe$_2$-based composites, particularly at high current densities.

To further elucidate the electrochemical behavior of the MoSe$_2$@MXene-30 composite, the cyclic voltammetry (CV) characteristics were investigated at different scan rates (Fig. 6a). The results indicate that the CV curves of MoSe$_2$@MXene-30 exhibit similar profiles at a scan rate in the range of 0.2–1 mV s^{-1}. The redox peak intensities gradually
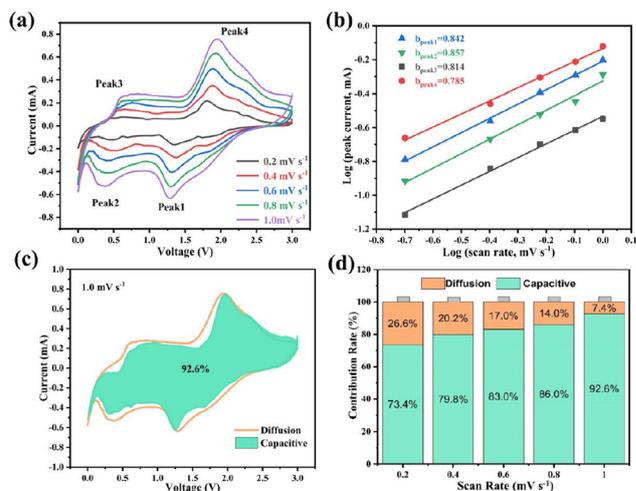

Fig. 6 Electrochemical test of the MoSe$_2$@MXene-30 composite: (a) CV curves at a scanning rate between 0.2 and 1 mV s^{-1}, (b) relationship between the peak current and the scan rate, (c) capacitive contribution curve at a scan rate of 1 mV s^{-1}, and (d) contribution rates at different scan rates.

increase with the increase in scan rate, accompanied by minor shape deformation. This suggests that the MoSe$_2$@MXene-30 composite possesses excellent rate performance. At a scan rate of 1 mV s^{-1}, the cathodic peaks (peak 1 and peak 2) are located at 1.3 V and 0.45 V, while the anodic peaks (peak 3 and peak 4) appear at 0.5 V and 2 V, respectively. Moreover, the area under the CV curve reflects the total capacity, which includes the contributions of diffusion-controlled and capacitive processes. The pseudo capacitive behavior of the electrode material can be evaluated using eqn (1) and (2):[49,50]

$$i = a\nu^b \quad (1)$$

$$\log i = b \log \nu + \log a \quad (2)$$

where ν represents the scan rate (mV s^{-1}), i denotes the total current (mA), and the characters a and b are adjustable parameters. The value of b was determined by the fitted slope of $\log i$ vs. $\log \nu$ plot. When the value of b is equal to 0.5 or 1, the electrochemical reaction is regarded as the diffusion-controlled process or surface-controlled pseudocapacitive process, respectively.[51,52] As shown in Fig. 6b, the values of b obtained from the linear fitting of the cathodic peaks (peak 1 and peak 2) are 0.842 and 0.857, respectively, whereas the values of b are 0.14 and 0.785 acquired from the anodic peaks (peak 3 and peak 4), respectively. These results illustrate that the MoSe$_2$@MXene-30 composite exhibits a significant pseudocapacitive behavior.[53] The proportions of the capacitive effects and diffusion-controlled contributions were calculated using eqn (3) and (4):[50,54]

$$i = k_1\nu + k_2\nu^{1/2} \quad (3)$$

$$i/\nu^{1/2} = k_1\nu^{1/2} + k_2 \quad (4)$$

The capacity is composed of diffusion contribution ($k_2\nu^{1/2}$) and capacitive control ($k_1\nu$).[55] As shown in Fig. 6c, the ratio of

capacitive contribution at a scan rate of 1.0 mV s^{-1} is as high as 92.6%. Moreover, Fig. 6d illustrates that the capacitive contribution gradually increases with the increase in scan rate. It indicates that the MoSe$_2$@MXene-30 composite exhibits dominant capacitive behavior at higher scan rates, which accounts for its excellent cycling stability and superior rate performance.

To evaluate the reaction kinetics of MoSe$_2$ and MoSe$_2$@MXene-30 electrodes, electrochemical impedance spectroscopy (EIS) measurements were performed in the frequency range of 0.01–10^5 Hz. Fig. 6a and b present the EIS results of the two electrodes for the third cycle and 1000th cycle, respectively. The Nyquist plots consist of three distinct regions: a semicircle in the high-frequency region representing the solid electrolyte interface (SEI) film resistance (R_f), a semicircle in the mid-frequency region assigned to the charge transfer resistance (R_{ct}) at the interface between the electrode and the electrolyte, and a sloped line in the low-frequency region indicative of ion diffusion resistance, also known as Warburg impedance (Z_w).[56] Additionally, R_s represents the electrolyte resistance.[57] The impedance parameters obtained using ZView software are summarized in Table 1.

It is revealed that the R_s values of both MoSe$_2$ and MoSe$_2$@MXene-30 remain nearly unchanged before and after the cycles, confirming that no electrolyte decomposition occurs during excessive charge–discharge processes. After 1000 cycles, the value of R_f for pristine MoSe$_2$ increases from 28.45 to 90.24 Ω, while MoSe$_2$@MXene-30 retains a relatively constant R_f value. It is suggested that MoSe$_2$@MXene-30 forms a robust SEI layer, whereas the SEI layer on pristine MoSe$_2$ tends to rupture and degrade during the cyclic processes.[58] MoSe$_2$@MXene-30 has obviously lower R_{ct} values than those of pristine MoSe$_2$ before and after the cycles, demonstrating that the incorporation of MXenes effectively enhances the conductivity of MoSe$_2$. There is a sharp increase in the value of R_{ct} for pristine MoSe$_2$ after the 1000th cycle, but only a slight increment in the R_{ct} value is seen for the MoSe$_2$@MXene-30 electrode. It is assumed that the incorporation of MXene relieves the collapse of the structure on account of the volume expansion during the electrochemical cyclings and improves the structural stability.[59,60] The SEM patterns of MoSe$_2$@MXene-30 after 1000 cycles are shown in Fig. S1k and l.† It is revealed that MoSe$_2$@MXene-30 still retains the hollow spherical structure and MoSe$_2$ is uniformly distributed on the surface of MXene spheres even after 1000 cycles. The highly stable struc-

ture of MoSe$_2$@MXene-30 not only enhances the cycling performance but also prolongs the lifespan.

The Na$^+$ diffusion coefficients were obtained from galvanostatic intermittent titration technique (GITT), as shown in Fig. 7c and d. The sodium-ion diffusion coefficient (D_{Na^+}) was calculated using eqn (5):[61,62]

$$D_{Na^+} = \frac{4}{\pi\tau}\left(\frac{n_m V_m}{S}\right)^2\left(\frac{\Delta E_s}{\Delta E_t}\right)^2 \tag{5}$$

where n_m, V_m, and S represent the number of moles (mol), molar volume (cm^3 mol^{-1}), and the electrode/electrolyte contact area (cm^2) of the tested sample, respectively. ΔE_s and ΔE_t correspond to the voltage changes (V) during steady-state and constant current discharge, respectively.[61] As shown in Fig. 7d, the value of D_{Na^+} for the MoSe$_2$ electrode ranges from $10^{-13.09}$ to $10^{-11.37}$ cm^2 s^{-1} when the discharge voltage is between 0 and 3 V, whereas the diffusion coefficient for the MoSe$_2$@MXene-30 electrode ranges from $10^{-11.87}$ to $10^{-9.11}$ cm^2 s^{-1}. Both curves exhibit the local minimum value of D_{Na^+} when the discharge voltage is at 0.55 V, 0.8 V, and 1.5 V. Around 1.5 V, some MoSe$_2$ in the composite undergoes the intercalation reaction with sodium ions to form a Na$_x$MoSe$_2$ intermediate. Further intercalations of sodium ions with the Na$_x$MoSe$_2$ intermediate are corresponding to the peak at potentials near 0.8 V and 0.55 V.[22,46] Eqn (6) and (7) describe the intercalation reactions:

$$MoSe_2 + xNa^+ + xe^- \rightarrow Na_xMoSe_2 \tag{6}$$

$$Na_xMoSe_2 + xNa^+ + xe^- \rightarrow Mo + xNa_2Se \tag{7}$$
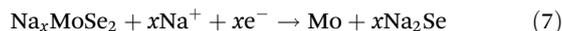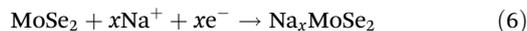
This is consistent with the analysis of the cyclic voltammetry (CV) tests discussed above. Clearly, the MoSe$_2$@MXene-30 electrode shows a higher value of D_{Na^+} than that of the MoSe$_2$ electrode, indicating that MoSe$_2$ nanoflakes anchored on

Table 1 Fitting results of the Nyquist plots of MoSe$_2$ and MoSe$_2$@MXene-30 at the 3rd and 1000th cycles

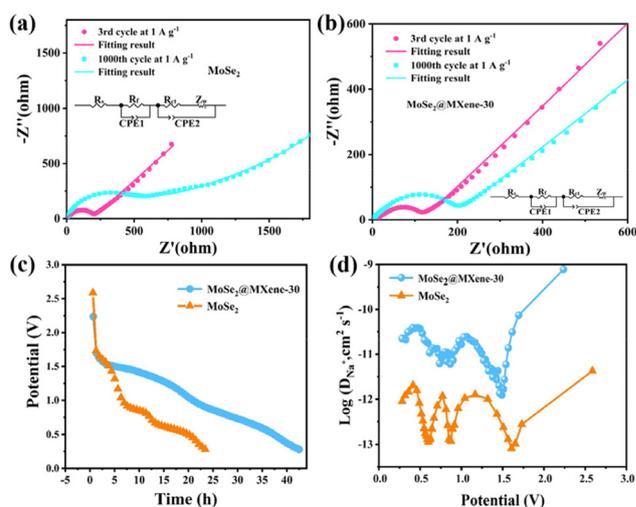| Cycle	MoSe$_2$		MoSe$_2$@MXene-30	
	3rd	1000th	3rd	1000th
R_s (Ω)	5.26	6.39	3.71	2.85
R_f (Ω)	28.45	90.24	10.8	15.45
R_{ct} (Ω)	160.6	446.2	96.5	160.1

Fig. 7 (a and b) Nyquist plots of MoSe$_2$ and the MoSe$_2$@MXene-30 composite after the 3rd and the 1000th cycles; (c) GITT discharge curves and (d) Na$^+$ diffusion coefficients of MoSe$_2$ and MoSe$_2$@MXene-30 electrodes.

MXene spheres provide more active sites for sodium ion reactions and facilitate the faster sodium ion intercalation reaction.

To better understand the impact of MXenes on the properties of $MoSe_2$, density functional theory (DFT) calculations were performed to simulate the physicochemical properties of the $MoSe_2$@MXene composite.[46] As depicted in Fig. 8a, pure $MoSe_2$ has a clear bandgap of 1.176 eV, indicating that $MoSe_2$ exhibits a typical semiconducting behavior. However, MXene and $MoSe_2$@MXene demonstrate a metallic behavior near the Fermi level, with a bandgap of zero, as shown in Fig. 8b and c. It is suggested that the introduction of MXene significantly enhances the electronic conductivity of $MoSe_2$. The density of states (DOS) for $MoSe_2$, MXene, and $MoSe_2$@MXene (Fig. 8d) are consistent with the band structure results. The patterns of the charge density difference for $MoSe_2$ and $MoSe_2$@MXene models are depicted in Fig. 8e. The brown and yellow electron clouds reflect the gain and loss of electrons, respectively. It is illustrated that for the $MoSe_2$@MXene composite, Se atoms in the Na–Se bond accumulate a substantial amount of electrons.[63] Furthermore, as shown in Fig. 8f, the adsorption energy of Na^+ on $MoSe_2$@MXene is −1.21 eV, which is lower than that of $MoSe_2$ (−1.16 eV). It is confirmed that the presence of MXenes can thermodynamically favor the adsorption of Na^+ on $MoSe_2$, thereby promoting Na^+ intercalation in the charge and discharge processes.[64]

Fig. 8 (a−c) Energy band structure of $MoSe_2$, MXene, and $MoSe_2$@MXene; (d) total density of states for $MoSe_2$, MXene and $MoSe_2$@MXene; (e) charge density differences of Na^+ adsorbed on $MoSe_2$ and $MoSe_2$@MXene; (f) adsorption energy of Na^+ adsorbed on the surfaces of $MoSe_2$ and $MoSe_2$@MXene models.

Conclusions

Hollow $MoSe_2$@MXene spheres with a unique $MoSe_2$ array structure were prepared by electrostatic adsorption and hydrothermal methods. The hollow structure not only alleviates structural damage due to volume expansion during cycling, but also enhances the electrolyte penetration and the contact area between the electrolyte and the active material. The presence of MXene and the unique $MoSe_2$ arrayed structure significantly improve the specific surface area and active sites for sodium-ion storage. Furthermore, the MXene obviously enhances the electrical conductivity of the $MoSe_2$@MXene series electrodes and accelerates the sodium-ion diffusion. $MoSe_2$@MXene-30 exhibits superior specific capacity and rate capability. At a current density of 1 A g^{-1}, the composite retained a specific capacity of 350.7 mA h g^{-1} during 1000 cycles with a capacity retention of 93.7%. The specific capacity is 261.1 mA h g^{-1} after 1000 cycles with a retention rate of 89.1% at a current density of 2 A g^{-1}. The specific capacities can still remain at 301, 268, and 230 mA h g^{-1} even at high current densities of 5.0, 7.0, and 10.0 A g^{-1}, respectively. $MoSe_2$ nanosheets *in situ* supported on the hollow MXene spheres show the potential prospects in sodium-ion battery electrodes.

Data availability

Data will be made available upon request.

Conflicts of interest

The authors declare that they have no conflict of interest.

Acknowledgements

References

1 M. Li, J. Lu, Z. Chen, *et al.*, 30 Years of lithium-ion batteries, *Adv. Mater.*, 2018, **30**(33), 1800561.

2 V. Palomares, P. Serras, I. Villaluenga, *et al.*, Na-ion batteries, recent advances and present challenges to become low cost energy storage systems, *Energy Environ. Sci.*, 2012, **5**(3), 5884–5901.

3 L. Ma, E. Z. Li, Z. B. Li, *et al.*, Electron-repulsion effect of anti-solvent strategy for long-cycle nickel sulfide-containing potassium-ion batteries, *Nano Energy*, 2024, 125.

4 P. K. Nayak, L. Yang, W. Brehm, *et al.*, From lithium-ion to sodium-ion batteries: advantages, challenges, and surprises, *Angew. Chem., Int. Ed.*, 2018, **57**(1), 102–120.
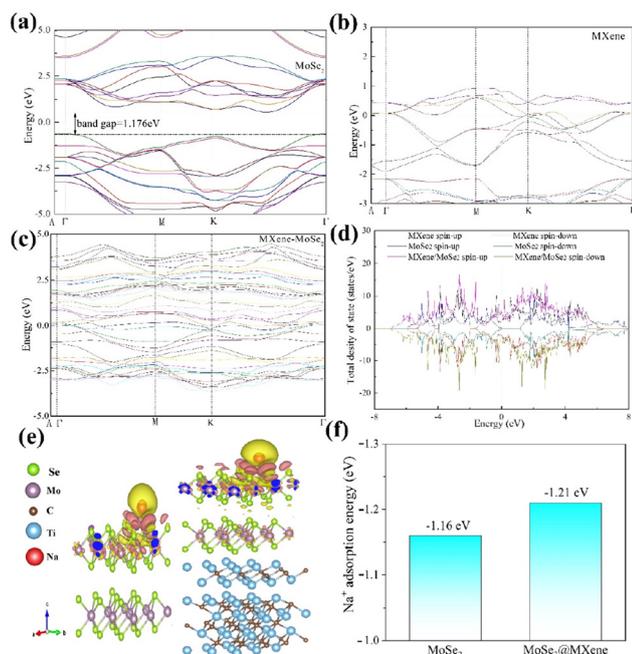
5 J. Y. Hwang, S. T. Myung and Y. K. Sun, Sodium-ion batteries: present and future, *Chem. Soc. Rev.*, 2017, **46**(12), 3529–3614.

6 Y. Li, J. Zhang, Q. Chen, *et al.*, Emerging of heterostructure materials in energy storage: a review, *Adv. Mater.*, 2021, **33**(27), 2100855.

7 D. Q. Chen, W. Zhang, K. Y. Luo, *et al.*, Hard carbon for sodium storage: mechanism and optimization strategies toward commercialization, *Energy Environ. Sci.*, 2021, **14**(4), 2244–2262.

8 Z. X. Huang, Z. Y. Gu, Y. L. Heng, *et al.*, Advanced layered oxide cathodes for sodium/potassium-ion batteries: development, challenges and prospects, *Chem. Eng. J.*, 2023, 452.

9 Y. You and A. Manthiram, Progress in high-voltage cathode materials for rechargeable sodium-ion batteries, *Adv. Energy Mater.*, 2018, **8**(2), 1701785.

10 T. Nagaura, J. L. Li, J. F. S. Fernando, *et al.*, Expeditious Electrochemical synthesis of mesoporous chalcogenide Flakes: mesoporous Cu_2Se as a Potential high-rate anode for sodium-ion battery, *Small*, 2022, **18**(34), 2106629.

11 N. Li, Y. F. Zhang, M. L. Jia, *et al.*, 1T/2H $MoSe_2$-on-MXene heterostructure as bifunctional electrocatalyst for efficient overall water splitting, *Electrochim. Acta*, 2019, 326.

12 Y. Dahiya, M. Hariram, M. Kumar, *et al.*, Modified transition metal chalcogenides for high performance supercapacitors: current trends and emerging opportunities, *Coord. Chem. Rev.*, 2022, 451.

13 K. B. Ibrahim, T. A. Shifa, S. Zorzi, *et al.*, Emerging 2D materials beyond mxenes and TMDs: Transition metal carbo-chalcogenides, *Prog. Mater. Sci.*, 2024, 144.

14 C. Lamiel, I. Hussain, H. Rabiee, *et al.*, Metal-organic framework-derived transition metal chalcogenides (S, Se, and Te): challenges, recent progress, and future directions in electrochemical energy storage and conversion systems, *Coord. Chem. Rev.*, 2023, 480.

15 L. H. Wang, L. L. Ren and Y. F. Qin, The review of hybridization of transition metal-based chalcogenides for lithium-ion battery anodes, *Materials*, 2023, **16**(12), 4448.

16 X. D. Li, J. L. Li, W. C. Zhuo, *et al.*, In situ monitoring the potassium-ion storage enhancement in iron selenide with ether-based electrolyte, *Nano-Micro Lett.*, 2021, **13**(1), 179.

17 X. Hu, W. Zhang, X. Liu, *et al.*, Nanostructured Mo-based electrode materials for electrochemical energy storage, *Chem. Soc. Rev.*, 2015, **44**(8), 2376–2404.

18 M. Luo, H. Yu, F. Hu, *et al.*, Metal selenides for high performance sodium ion batteries, *Chem. Eng. J.*, 2020, 380.

19 Y. Tan, M. Yi, Z. Zhu, *et al.*, Carbon-coated $MoSe_2$/MXene heterostructures as active materials for high-performance Na^+ batteries, *Mater. Today Commun.*, 2022, 31.

20 Y. Tang, Z. Zhao, Y. Wang, *et al.*, Carbon-stabilized interlayer-expanded few-layer $MoSe_2$ nanosheets for sodium ion batteries with enhanced rate capability and cycling performance, *ACS Appl. Mater. Interfaces*, 2016, **8**(47), 32324–32332.

21 Z. A. Zhang, Y. Fu, X. Yang, *et al.*, Hierarchical $MoSe_2$ nanosheets/reduced graphene oxide composites as anodes for lithium-ion and sodium-ion batteries with enhanced electrochemical performance, *ChemNanoMat*, 2015, **1**(6), 409–414.

22 Y. F. Chao, S. H. Jia, J. Z. Li, *et al.*, A dual heterostructure enables the stabilization of 1T-rich $MoSe_2$ for enhanced storage of sodium ions, *Chem. Sci.*, 2024, **15**(28), 11134–11144.

23 H.-C. Fu, V. Ramalingam, H. Kim, *et al.*, MXene-contacted silicon solar eells with 11.5% efficiency, *Adv. Energy Mater.*, 2019, **9**(22), 1900180.

24 S. Seyedin, S. Uzun, A. Levitt, *et al.*, MXene composite and coaxial fibers with high stretchability and conductivity for wearable strain sensing textiles, *Adv. Funct. Mater.*, 2020, **30**(12), 1910504.

25 X. Zeng, C. Zhao, X. Jiang, *et al.*, Functional tailoring of multi-dimensional pure MXene nanostructures for significantly accelerated electromagnetic wave absorption, *Small*, 2023, **19**(41), 2303393.

26 P. Ma, D. Fang, Y. Liu, *et al.*, MXene-Based materials for electrochemical sodium-ion storage, *Adv. Sci.*, 2021, **8**(11), 2003185.

27 X. Chen, J. Zhu, J. Cai, *et al.*, Nanosheets assembled layered MXene/$MoSe_2$ nanohybrid positive electrode materials for high-performance asymmetric supercapacitors, *J. Energy Storage*, 2021, 40.

28 M. Q. Zhao, X. Q. Xie, C. E. Ren, *et al.*, Hollow MXene spheres and 3D macroporous MXene frameworks for Na-ion storage, *Adv. Mater.*, 2017, **29**(37), 1702410.

29 C. Chen, J. Chen, W. Yang, *et al.*, MoS_2 nanosheet arrays in situ grown on hollow MXene sphere as an advanced anode material for sodium-ion batteries, *J. Energy Storage*, 2024, 100.

30 G. Kresse and D. Joubert, From ultrasoft pseudopotentials to the projector augmented-wave method, *Phys. Rev. B: Condens. Matter Mater. Phys.*, 1999, **59**(3), 1758–1775.

31 K. Mathew, V. S. C. Kolluru, S. Mula, *et al.*, Implicit self-consistent electrolyte model in plane-wave density-functional theory, *J. Chem. Phys.*, 2019, **151**(23), 234101.

32 S. Ren, X. Pan, Y. Zhang, *et al.*, Conductive MXene/Polymer composites for transparent flexible supercapacitors, *Small*, 2024, **20**(35), 2401346.

33 Y. Wang, X. Wang, X. Li, *et al.*, Engineering 3D ion transport channels for flexible MXene films with superior capacitive performance, *Adv. Funct. Mater.*, 2019, **29**(14), 1900326.

34 K. Lv, J. Z. Zhang, X. Zhao, *et al.*, Understanding the effect of pore size on electrochemical capacitive performance of MXene foams, *Small*, 2022, **18**(27), 2202203.

35 X. T. Xing, Y. T. Sui, Q. S. Li, *et al.*, Multifunctional ZnAl-MoO_4 LDH assembled $Ti_3C_2T_x$/MXene composite for active/passive corrosion protection behavior of epoxy coatings, *Appl. Surf. Sci.*, 2023, 623.

36 X. H. Zhang, M. Q. Xue, X. H. Yang, *et al.*, Hydrothermal synthesis and tribological properties of MoSe$_2$ nanoflowers, *Micro Nano Lett.*, 2015, **10**(7), 339–342.

37 K. She, Y. Huang, W. Fan, *et al.*, 3D flower-like hollow MXene@MoS$_2$ heterostructure for fast sodium storage, *J. Colloid Interface Sci.*, 2024, **656**, 270–279.

38 S. H. Yang, Y. J. Lee, V. Kang, *et al.*, Carbon-coated three-dimensional MXene/Iron selenide ball with core-shell structure for high-performance potassium-ion batteries, *Nano-Micro Lett.*, 2022, **14**(1), 17.

39 S. Adomaviciute-Grabusove, A. Popov, S. Ramanavicius, *et al.*, Monitoring Ti$_3$C$_2$T$_x$-MXene degradation pathways ssing raman spectroscopy, *ACS Nano*, 2024, **18**(20), 13184–13195.

40 Z. Y. Yuan, J. M. Cao, S. Valerii, *et al.*, MXene-bonded hollow MoS$_2$/carbon sphere strategy for high-performance flexible sodium ion storage, *Chem. Eng. J.*, 2022, **430**.

41 X. Wu, Z. Wang, M. Yu, *et al.*, Stabilizing the MXenes by carbon nanoplating for developing hierarchical nano-hybrids with efficient lithium storage and hydrogen evolution capability, *Adv. Mater.*, 2017, **29**(24), 1607017.

42 L. Zhao, B. Dong, S. Li, *et al.*, Interdiffusion reaction-assisted hybridization of two-dimensional metal-organic frameworks and Ti$_3$C$_2$T$_x$ nanosheets for electrocatalytic oxygen evolution, *ACS Nano*, 2017, **11**(6), 5800–5807.

43 X. Zhang, H. Shi, L. Liu, *et al.*, Construction of MoS$_2$/MXene heterostructure on stress-modulated kapok fiber for high-rate sodium-ion batteries, *J. Colloid Interface Sci.*, 2022, **605**, 472–482.

44 Q. Q. Jiang, W. F. Zhao, X. Y. Xu, *et al.*, Architecting carbon-coated Mo$_2$CT$_x$/MoSe$_2$ heterostructures enables robust potassium storage, *Chem. Commun.*, 2023, **59**(89), 13329–13332.

45 H. Huang, J. Cui, G. Liu, *et al.*, Carbon-coated MoSe$_2$/MXene hybrid nanosheets for superior potassium storage, *ACS Nano*, 2019, **13**(3), 3448–3456.

46 E. Xu, Y. Zhang, H. Wang, *et al.*, Ultrafast kinetics net electrode assembled via MoSe$_2$/MXene heterojunction for high-performance sodium-ion batteries, *Chem. Eng. J.*, 2020, **385**.

47 F. R. Qin, H. X. Hu, Y. J. Jiang, *et al.*, Mesoporous MoSe$_2$/C composite as anode material for sodium/lithium ion batteries, *J. Electroanal. Chem.*, 2018, **823**, 67–72.

48 W. X. Cheng, T. T. Mao, Y. Z. Chen, *et al.*, 0*In situ* synthesis and application of hollow H-SnS/MXene@C nanobox for advanced LIBs and NIBs anodes, *J. Energy Storage*, 2024, **84**.

49 X. Deng, Z. Wei, C. Cui, *et al.*, Oxygen-deficient anatase TiO$_2$@C nanospindles with pseudocapacitive contribution for enhancing lithium storage, *J. Mater. Chem. A*, 2018, **6**(9), 4013–4022.

50 X. Dong, Z. Xing, G. Zheng, *et al.*, MoS$_2$/N-doped graphene aerogles composite anode for high performance sodium/potassium ion batteries, *Electrochim. Acta*, 2020, **339**.

51 V. Augustyn, J. Come, M. A. Lowe, *et al.*, High-rate electrochemical energy storage through Li$^+$ intercalation pseudocapacitance, *Nat. Mater.*, 2013, **12**(6), 518–522.

52 Q. H. Nguyen, H. Kim, I. T. Kim, *et al.*, Few-layer NbSe$_2$@graphene heterostructures as anodes in lithium-ion half- and full-cell batteries, *Chem. Eng. J.*, 2020, **382**.

53 J. Wang, J. Polleux, J. Lim, *et al.*, Pseudocapacitive contributions to electrochemical energy storage in TiO$_2$ (anatase) nanoparticles, *J. Phys. Chem. C*, 2007, **111**(40), 14925–14931.

54 D. Chao, C. Zhu, P. Yang, *et al.*, Array of nanosheets render ultrafast and high-capacity Na-ion storage by tunable pseudocapacitance, *Nat. Commun.*, 2016, **7**.

55 J. B. CoOk, H.-S. Kim, Y. Yan, *et al.*, Mesoporous MoS$_2$ as a transition metal dichalcogenide exhibiting pseudocapacitive Li and Na-Ion charge storage, *Adv. Energy Mater.*, 2016, **6**(9), 1501937.

56 H. Yang, R. Xu, Y. Gong, *et al.*, An interpenetrating 3D porous reticular Nb$_2$O$_5$@carbon thin film for superior sodium storage, *Nano Energy*, 2018, **48**, 448–455.

57 J. Kim, D. Kim, I. Lee, *et al.*, Bulk concentration dependence of electrolyte resistance within mesopores of carbon electrodes in electric double-layer capacitors, *Bull. Korean Chem. Soc.*, 2016, **37**(2), 213–218.

58 J. M. Tao, Z. R. Yan, D. Y. Wang, *et al.*, Rational designing of MoSe$_2$ nanosheets in carbon framework for high-performance potassium-ion batteries, *Chem. Eng. J.*, 2022, **448**.

59 Y. Liu, M. Zhu and D. Chen, Sheet-like MoSe$_2$/C composites with enhanced Li-ion storage properties, *J. Mater. Chem. A*, 2015, **3**(22), 11857–11862.

60 X. Zhao, W. Cai, Y. Yang, *et al.*, MoSe$_2$ nanosheets perpendicularly grown on graphene with Mo-C bonding for sodium-ion capacitors, *Nano Energy*, 2018, **47**, 224–234.

61 Y. Wang, Y. Zhang, H. Li, *et al.*, Realizing high reversible capacity: 3D intertwined CNTs inherently conductive network for CuS as an anode for lithium ion batteries, *Chem. Eng. J.*, 2018, **332**, 49–56.

62 P. G. Bruce, S. A. Freunberger, L. J. Hardwick, *et al.*, Li-O$_2$ and Li-S batteries with high energy storage (vol 11, pg 19, 2012), *Nat. Mater.*, 2012, **11**(2), 172.

63 A. Kokalj, XCrySDen - a new program for displaying crystalline structures and electron densities, *J. Mol. Graphics Modell.*, 1999, **17**(3–4), 176.

64 Q. Tang, Z. Zhou and P. Shen, Are MXenes promising anode materials for Li ion batteries? computational studies on electronic properties Ti$_3$C$_2$ and Ti$_3$C$_2$X$_2$ Li storage capability of and (X = F, OH) monolayer, *J. Am. Chem. Soc.*, 2012, **134**(40), 16909–16916.